The Effect of CO_2-Induced Dissolution on Flow Properties in Indiana Limestone: an *In Situ* Synchrotron X-Ray Micro-Tomography Study

Marco Voltolini[1] and Jonathan Ajo-Franklin[1]

[1] Lawrence Berkeley National Laboratory

Abstract

The injection of CO_2-rich fluids in carbonate rocks results in an evolution of the pore space, with consequent changes in the hydraulic properties of the reservoir; how these properties evolve, particularly for parameters relevant to multiphase flow e.g. $P_c(s)$, remains a topic of active research despite several decades of study. We have carried out an *in situ* synchrotron X-ray microtomography experiment to monitor pore structure evolution during dissolution of an Indiana Limestone core; the experiment involved flowing CO_2-saturated water through the core for 36 hours and resulted in 10 volumes corresponding to different temporal stages of the dissolution process. The injection parameters corresponded to the flow velocities expected near the well-bore region of a shallow aqueous CO_2 injection; fast flow rates with high reactant availability. Analysis of the tomographic data shows flow-enhanced dissolution i.e. channeling, and provides a time-resolved map of pore space alteration. Using the resulting 4D pore space volume, we modeled the evolution of capillary-pressure curves; this exercise demonstrates how pore structure evolution could impact the invasion and remobilization of non-wetting fluids, dramatically decreasing the entry pressure and the P_C in some parts of the sample. The modeling of permeability, using a Stokes solver approach, quantified the relationship of porosity vs. permeability; we found that a modest increase in porosity, especially when the channeling system is more developed, greatly affects permeability. These results demonstrate how movement of CO_2 saturated brine near injected plumes might alter drainage dynamics near the plume boundary, thus leading to mobilization across subtle capillary barriers.

Keywords: *Limestone dissolution; In-situ synchrotron X-ray microtomography; Porosity evolution; Capillary pressure modeling; Permeability modeling.*

1. Introduction

Geological carbon sequestration (GCS) is current strategy under development for greenhouse gas emission mitigation at an industrial scale. Different approaches for GCS are currently being studied, with a variety of targets for reservoir rocks, typically deep aquifers and depleted oil and gas fields (e.g. Benson and Cole, 2008). In situations where CO_2 value is required for injection and appropriate fields exist near sources, CO_2 enhanced oil recovery (EOR) is an attractive transition strategy. Besides the more "typical" reservoir rocks, usually chosen because their injectivity, proximity, and suitable stratigraphic settings, some rocks with advantageous qualities such as high reactivity, typically volcanic or volcanoclastic reservoir rocks, are also targeted in specific regions (e.g. Mc Grail et al., 2006; Gislason and Oelkers, 2014; general for basalts. Zhang et al., 2015; for volcanogenic sandstones).

GCS relies on four main primary trapping mechanisms: i) structural trapping, where a sealing formation stops the migration of CO_2, acting as a barrier. ii) capillary trapping, where the CO_2 is trapped by capillary forces in the fluids after the imbibition following the CO_2 injection; iii) solubility trapping, where CO_2 is dissolved in the brine of the reservoir; iv) mineral trapping, where the CO_2 reacts with minerals in the reservoir to precipitate as carbonates (Benson et al., 2005). These mechanisms can be present, and interact, at different times and space in the targeted reservoir and depends on a wide variety of factors, including rock mineralogy, microstructure, and hydraulic properties. Beyond primary structural seals on a GCS reservoir, numerous more subtle low/intermediate permeability features often exist, referred to as "baffles" in clastic systems, which can control larger scale $scCO_2$ distribution and timescales for mixing and dissolution e.g. examples include thin shales (e.g. Cavanagh and Haszeldine, 2014) and marls in carbonate sequences.

A significant fraction of the targeted storage formations, particularly in an EOR context, are carbonates, or at least carbonates-rich rocks with examples including the Weyburn field (White, 2013) and EOR in the Permian Basin. Carbonates (typically calcite and/or dolomite) readily react with the acidified brine (Peng et al., 2015, for calcite; Baritantonaki et al., 2017, for dolomite). The reactions induced by the acidified fluids can modify the microstructure of the reservoir rock, altering its hydraulic, geochemical, and geomechanical properties (e.g. Mohamed and Nasr-El-Din, 2012), as well as damage the injection wells (e.g. Carroll et al., 2017) and immediate surroundings.

How a reservoir carbonate rock will evolve in a GCS scenario depends on the combination of a wide range of factors, all tightly coupled. Pressure, temperature, and salinity control the maximum amount of CO_2 that can be dissolved in the brine. The mineralogy of the reservoir rock controls its reactivity (e.g. calcite dissolves faster than dolomite, as shown in Deng et al., 2016). The microstructure of the rock (pore-size distribution, crystallinity of the mineral phases, etc.) also has a significant impact on the reactivity of the rock and its evolution (Deng et al., 2016, 2017). The hydraulic properties can exert control on the evolution of the microstructure, e.g. leading towards wormholing, channeling, or more homogeneous dissolution patterns (Ott and Oedai, 2015). Last, the mechanical properties of a rock can be weakened by the dissolution, and cause localized compaction (Grgic, 2011).

Given the complexity of this tightly interconnected system, the modeling of the phenomena, from pore to basin scales, which is needed to predict the evolution of the system during and after the injection, becomes extremely challenging. The first step needed is to identify and quantify the relevant phenomena at the pore scale, including the time evolution of porosity, permeability, and multi-phase parameters (e.g. relative permeability and P_C (s)). In this context, a technique such as in-situ X-ray micro computed tomography (XR-µCT) can provide the information required. XR-µCT, when properly utilized, has the capacity to observe the evolution of rock microstructure in 3D while reactions occur. In contrast, many traditional petrographic techniques are inherently 2D and destructive. The 3D nature of tomographic data can also be used for the characterization of the pore space in a quantitative fashion (e.g. Ji et al., 2012, for Indiana limestone), or to calculate hydraulic properties in a context of digital rock physics (Knackstedt et al., 2009; Andrä et al., 2013). The ability of this technique to provide key parameters in hydrogeochemical processes is highlighted by the substantial number of recent studies targeting the topic of CO_2-induced dissolution in carbonate rocks of interest for GCS, either in the context of reservoir or caprock performance (Gouze and Luquot 2011; Menke et al., 2015, 2016; Ott and Oedai, 2015; Deng et al., 2016, 2017).

Our study aims to understand the dissolution patterns in a generic carbonate reservoir rock with a microstructure and mineralogy compatible with GCS/EOR targeted reservoir rocks. This experiment is compatible with the scenario of a near-wellbore region, wherw the availability of reactant is high and the flow is fast. This is the situation where the evolution is expected to be the fastest and the most pervasive, and where analogous microstructural changes, when occurring in deep reservoirs, translate in changes in permeability and entry pressure that might play a key role in the distribution of the CO_2 during the injection process. We explore how such a system might evolve from a microstructural perspective, its implications on the hydraulic properties of the rock, and how these can potentially impact the injection of CO_2.

2. Materials and Methods

2.1. Sample characterization and preparation

For our in-situ synchrotron X-ray micro-computed tomography (SXR-µCT) study, a mini core of the Indiana Limestone (from a quarry in the Bedford area) was selected (*Kocurek Industries*). The Indiana Limestone is part of the Salem Formation (Mississippian) and is currently actively quarried (Indiana Limestone handbook, 2007) and is actively utilized in core-flood and rock physics studies. The sample displays the microstructure of an organogenic limestone, with a complex history of recrystallization of the carbonates and silica from the original deposition. The textures typical of organogenic $CaCO_3$ are clearly present (fragments of foraminifera, bryozoa, etc.) giving the rock a typical appearance and a very complex porosity structure at different scales. X-ray powder diffraction highlights that the sample is composed almost entirely of calcite, with trace amounts of quartz and clays (both <1% by weight, as per Rietveld analysis).

The complexity of the microstructure of the Indiana Limestone at different scales is exemplified in Fig. 1, where SEM images at different resolutions are shown. At the millimeter scale (Fig. 1a) the backscattering image of a cut section highlights the main microstructure of the rock: the main components are oolitic structures (often with a bioclast as the nucleus) cemented together, with an interstitial pore space. When progressively increasing the magnification, as shown in the sequence of secondary electrons images in Fig. 1b,c,d, a new hierarchy of structures is visible. The ooliths retain most of their original shape, and display the characteristic concentric accretion layered structure. When looking at the single layers, it is possible to observe that the layers are composed of calcite microcrystals. In some layers, these crystals are below one micron in size (detail of a detached single layer in Fig. 1c). Few isolated perfectly euhedral quartz crystals are present as well, as an accessory phase, highlighting the complex recrystallization history of the rock. This microstructure is expected to have a direct impact on the porosity of the system (as emphasized by Freire-Gormaly et al, 2015), and at the scale considered we can identify two main different porosity segments: i) the interstitial porosity (which is above the resolution of the SXR-µCT measurement) generated by the aggregation structure of the ooliths, and ii) the micro-/nano- porosity generated by the space among the single micro-/nano- calcite crystals, which is below the resolution of the SXR-µCT measurement. This porosity distribution has potentially a significant impact in the estimate of all the chemical processes depending on the reactive surface area values.

The dimensions of the sample used for the in situ SXR-µCT experiment was a cylindrical core, 8.6 mm in diameter × 7.7 mm in height, fully imaged during the experiment; the full volume image enabled recovery of appropriate boundary conditions for subsequent flow modeling.

2.2. SXR-µCT measurement and first data processing

The Indiana Limestone mini-core was placed between two threadless 3/8” stainless steel fittings with 1/8” tubing male inlets, and jacketed using polyvinylidene fluoride heat-shrink tubing, locked in place on the threadless portion of the fittings, and fixed with steel wire. The jacketed sample was connected to a high performance liquid chromatography pump set at 0.2 ml/min constant flow. The sample was first flushed with He, and then saturated with water to collect the baseline dataset. A stirred reservoir filled with water and a headspace of CO_2 kept at ~11 psi (76 kPa) and 28 °C, and equilibrated overnight, was used to provide the CO_2 aqueous solution to flow through the sample. That pressure was maintained in the flow system via a back-pressure regulator.

The SXR-µCT scans were conducted every 4 hours, providing a total of 10 datasets covering 36 hours of effective reaction. The SXR-µCT experiments were carried out at beamline 8.3.2. (MacDowell et al., 2012) at the Advanced Light Source (ALS), Lawrence Berkeley National Laboratory (LBNL). The beamline setup for this experiment used filter-hardened (2 mm Al, and 0.5 mm Cu) white light as the radiation source. For this kind of experiments the use of white light compared to the monochromatic one is advantageous for several reasons, including faster data collection, thus minimizing eventual motion artifacts in dynamic experiments, and a larger

vertical field of view. For each time step, a total of three vertical tiles were collected, to image the entire sample height. During each tomographic data collection we acquired 1441 projections over a 180 degrees rotation. The exposure time varied from 55 ms to 95 ms, increasing in time to compensate for the browning of the objective lens of the detector system, due to radiation-induced color centers generation in the glass. The detector system included a 50 µm Ce:LuAG scintillator, 2× objective optics, and a PCO-4000 CCD camera. The resulting pixel size was 4.4 µm. The sample to detector distance was ~5 cm. The tomographic datasets were reconstructed using the standard filtered backprojection approach, with a Shepp-Logan filter (Kak and Slaney, 2001), as implemented in the software Octopus® (Dierick et al., 2004).

2.3. Tomographic Data processing and analysis

The reconstructed volumes were analyzed using the Fiji software framework (Schindelin et al., 2012). The first processing step after reconstruction was the segmentation of the pore space from the solids. The Otsu thresholding algorithm (Otsu, 1979) was used to separate the two classes of objects. The volume data 3D visualization was carried out using the VG Studio® 2.0 software. A cylindrical cropping of the volumes, to cut the inlet and outlet steel fitting ends and the jacket, was also done to obtain a cylinder with only the rock sample. Given the precise coring and mounting of the sample, only a very small amount (~100 µm) of sample was cut during the cropping procedure. No evidence of preferential flow along the jacket, or any other anomalous behavior, was observed in the extracted imagery. The segmented volumes were used for the first pore space analysis, with a slice-by-slice porosity calculation to highlight the localization of the dissolution, i.e. the extent of dissolution in function of the distance from the inlet. The Local Thickness (LT) approach (Dougherty and Kunzelmann, 2007) was chosen to analyze the evolution of the pore space during the reaction, since it is easy to calculate, does not require an artificial distinction between pores and throats, and provides useful information about which class of features evolve. The same LT attribute is the starting point for the digital rock physics model we use to calculate drainage behavior.

2.3.1. Modeling the evolution of the capillary pressure curves

Once the pore space local thickness volumes for each time step have been calculated, we calculate the capillary pressure curves for a perfectly non-wetting fluid following the approach described in Voltolini et al. 2017, where we refer the reader for the details; this approach is based on the maximum inscribed spheres concept as presented by Silin et al., 2011. The main advantages of this approach are that it is fast to calculate, it needs only a binary volume of the pore space as a starting point, and has already proved effective in modeling both the 3D distribution of supercritical CO_2 at reservoir conditions, and mercury intrusion pycnometry curves, albeit with a smaller range of porosity values, limited by the resolution of the imaging setup. The approach is purely geometrical in nature which makes it straightforward to implement and computationally efficient. The main limitation is that it neglects several factors including (i) the contact angle of the invading fluid, which is always considered perfectly non-wetting and (ii) dynamic effects

present at high capillary numbers. This first limitation is negligible when simulating the very first stage of drainage of $scCO_2$ in markedly water-wet systems (as we consider the one presented in this work), or Hg intrusion (as demonstrated in Voltolini et al. 2017), but cannot be used on systems with partial, evolving, or mixed, wettability.

2.3.2. Modeling the evolution of the permeability

With the dissolution of the calcite during the experiments, the evolution of the pore space should clearly impact the permeability of the system. Giving the challenges of experimental permeability measurements on mm dimension samples, we decided to use a modeling approach to retrieve permeability from the 4D volumes. The permeability in the different datasets was calculated using a Stokes flow solver, similar to the one published in Silin and Patzek (2009), as presented in Zuo et al., (2017) which utilized the same implementation we selected. The permeability calculation has been carried out on 250 vx cubic subvolumes of the sample, rescaled at 17.6 um per vx, resulting in a cube with a 4.4 mm side, including most of the measured sample. This approach is not only helpful to estimate the evolution of the permeability, but the generation of the velocity fields also allows better visualization of the presence and time evolution of preferential flowpaths.

3. Results and discussion

The first step in analyzing the results is a qualitative inspection of the volume renderings of sequential SXR-µCT reconstructions. In Fig. 2, two full sequences of the volume renderings are presented, with each time step being 4h, with the top half showing a vertical virtual cut, while the bottom half shows a horizontal cut about 1 mm from the inlet, viewed from the top (inlet). The evolution of the microstructure of the sample is clear, highlighted by the increase in porosity with time. This increase in porosity seems clearly more pronounced closer to the inlet, as can be seen from the vertical cut sequence. From the horizontal section, it is possible to identify which parts of the sample dissolve preferentially; the small features, such as thin fragments, and detached/isolated oolite layers seem to dissolve faster than the more “blocky” parts of the sample such as the solid oolites. This is to be expected, assuming equal reactant availability conditions, given the different reactive surface area available. In addition, some pores display faster dissolution rates than others, hinting at issues of different reactant supply controlled by preferential flowpaths. Both sample microstructure (more reactive surface area induces faster dissolution) and hydraulics (faster reactant supply causes faster dissolution) involve the local reaction rate of the material and the subsequent dynamic modification of the flowpaths.

Following these general observations, we can more precisely visualize the evolution, highlighting where and when the dissolution process occurred. One approach is to build a volume where the dissolved material is color-labeled with respect to time, providing a map of sequential dissolution surfaces This is carried out by using a XOR operator on each binary volume (pore space) with the previous one in the dissolution sequence, after volume registration, and finally color-label the result of each cycle and build a single volume. In Fig. 3 captures the dissolution process using this type of visualization: a thin (~250 µm) vertical slice of the volume has been virtually

cut, and on the left the volume rendering of the sample at the end of the experiment has been superimposed with the color-labeled volume representing the dissolved material. In the right panel of Fig. 3, only the latter volume is shown, for clarity. The use of a thin section of the sample helps to better appreciate the local features in such a complex microstructure. From this volume more precise information can be obtained. The material dissolved at the early stages (e.g. the blue color represents the material dissolved in the first 4 hours) is often associated with pore-filling calcite with a large apparent surface area or thin detached oolite laminae (similar to the one in Fig. 1c). This dissolution pattern can be seen in Fig. 3 where the blue-labeled regions, representing regions dissolved in the first 4-8 hours, are dominated by interstitial calcite regions. Often this material displays a slightly darker graylevel, i.e. it is less X-ray attenuating. Since the sample consists almost entirely of calcite, the darker graylevels are due to partial volume effects induced by sub-resolution micro/nanoporosity. Considering the more rapid dissolution in these regions, such nanoporosity is likely linked to higher local reactive surface areas.

As we follow the color code of the look-up table in Fig. 3 approaching the end of the reaction, we can see that the dissolution tends to concentrate on a specific population of pores (orange-red-white colors); in other pores the dissolution stops or proceeds very slowly. This is evidence of the evolution of the hydraulic properties of the sample generated by the dissolution: as dissolution proceeds, the creation of preferential flowpaths tends to progressively concentrate the reaction in those specific parts of the sample. This phenomena of localized preferential dissolution, referred to as wormholing, channeling, etc. have been observed several times in reactive transport experiments in carbonates (Fredd and Fogler, 1998; Siddiqui et al, 2006; Menke et al., 2016).

To describe the evolution of the pore space in a more quantitative fashion, we evaluated porosity on a slice-by-slice basis to examine dissolution trends across the sample. In Fig. 4a the slice-by-slice porosity plots are shown, following the orientation of the volume rendering figures (inlet at the top). A first observation is that during the initial 4 hours, the dissolved volume was larger than in the following time increments. This behavior can also be observed in Fig. 3 where the blue color is more prevalent than the others. Combining the information from the two figures we can develop a hypothesis: during the first stages of dissolution, strong preferential pathways are not developed, hence the dissolution of reactive material is more uniform. In addition to that, at the first stage more material with large reactive surface areas (isolated/detached oolite lamellae, loose “powdery” calcite, etc.), and therefore with faster dissolution rates, is present as well. With a more homogeneous flow, and the larger availability of reactive components, it is not surprising to observe a faster dissolution rate at the first stage of the experiment. The second observation from Fig. 4a is that net dissolution decreases as function of the distance from the inlet.

Another feature that can be observed from Fig. 4a is the presence of specific zones with higher dissolution rates. When looking at the porosity curves around slice #100, the plot in the unreacted sample is rather flat. While the reaction proceeds, particularly during the first 8 hours, it is possible to observe the generation of a new peak, meaning higher amounts of

dissolved materials and subsequent porosity is localized in that sample region. These newly formed peaks highlight portions of the sample where the dissolution was faster, and seem to be unrelated to porosity features present in the unreacted rock, i.e. they do not depend on the starting porosity value. Again, this behavior is likely due mostly to the presence of materials with textures resulting in high RSA values and the existence of preferential flowpaths enhancing local dissolution.

An alternative approach to evaluating pore space evolution is examination of local thickness histograms, an unbiased view of pore dimension modification. Fig. 4b depicts the time evolution of local thickness; as can be seen, the dominant process is an increase in abundance of small to intermediate size pores/throats in the 10-30 micron range. As the dissolution continues, flow localization results in larger dissolution features, shifting the newly created porosity to larger thickness/diameter values. The progressive nature of this phenomenon (the higher the reaction extent, the larger the size of the local thickness fraction that grows) is also observable at the “shoulder” of the curves, growing more and more towards the large local thickness values. This type of analysis suggests that local thickness is an excellent geometric proxy for tracking the evolution of channeling in an evolving porous system.

The behavior observed in both porosity and LT analysis, with the generation of preferential flowpaths getting larger with the evolution of the system, is a channeling behavior observed in Menke et al., 2017 in a similar experiment involving CO_2-induced dissolution in limestone samples. The characteristic evolution of the pore space in such reactive systems can be, in theory, inferred by understanding the system in terms of the dimensionless Damkhöler and Péclet numbers, representing the ratios of advection to reaction, and the diffusion to advection times, respectively. The two numbers have been calculated following Menke et al. (2017); we adopt the following formulas for consistency,

$$Da = \frac{\pi r}{U_{av} n} \quad (1)$$

$$Pe = \frac{U_{av} L}{D} \quad (2)$$

where r is the reaction rate for calcite, as measured at similar P/T conditions in Plummer et al. (1978) and U_{av} is the average velocity of the fluid in the pore space (as derived from the Stokes flow model). Likewise, n is defined as $\rho_{Cc}(1-\phi)/M_{Cc}$, where ρ_{Cc} is the density of pure calcite, ϕ is the total porosity, and M_{Cc} is the molecular mass of calcite. The value of the porosity used here is the one obtained via the tomographic dataset, therefore the nanoporosity present in the sample is not accounted for. L is the characteristic length defined as π/SA, where SA is the surface area. The SA has been calculated by measuring the total surface of the pore space from the tomographic dataset, corrected with the roughness of the surface of an oolite as measured via SEM imaging, at higher resolution, to take into account the granular nature of the surfaces. A roughness correction factor R_C = 72.8 has been applied to the

surface area value calculated from the tomographic dataset to derive the SA. This correction should, at least partially, take into account the features below the SXR-μCT resolution that can potentially have a significant effect on the dissolution rates of the material. Based on these assumptions, the values found for the starting sample were: $Da = 3.9 \bullet 10^{-4}$ and $Pe = 3.3 \bullet 10^{3}$. A low value for *Da* suggests a state where the reaction rate is slow compared to the advection, and a high *Pe* indicates that advection dominates compared to diffusion, a condition compatible with the development of channels observed in the experiment. These values seem to agree also with the values found in Menke et al. (2016), given the different experimental conditions (and samples) and the different methods used to estimate ϕ and SA.

3.1. Evolution of capillary pressure distribution: effects on drainage

The localized dissolution of the sample during flow and reaction, as described in the previous section, is expected to modify hydraulic properties. The first topic addressed in this context is the evolution of the drainage properties of the rock. When considering GCS and/or EOR scenarios, such an evolution of the pore space can have a significant impact on the entry pressure of a non-wetting fluid (such as supercritical CO_2 or oil). This variation in entry pressure could modify the $scCO_2$ migration pathways in a reservoir by enabling plume expansion into regions initially., The measurement of capillary pressure (P_C) curves is commonly estimated using Hg intrusion pycnometry. Hg pycnometry is a destructive test and hence cannot be used to monitor evolution of a pore system during reaction. As we presented in Voltolini et al. (2017) and had been earlier proposed in Silin et al. (2011), we have developed a code enabling calculation of P_C curves using tomographic datasets only; consequently, the approach can be applied to a sequence of volumes from dissolution experiments to probe alteration of parameters such as entry pressure. It is worth emphasizing that this digital rock physics approach, even with intrinsic limitations such as resolution and field of view constraints, enables virtual measurements that could not be executed experimentally.

We imposed the top of the sample as the inlet boundary (as in the real experiment); for each dataset, we calculated the invaded volumes as a function of the decrease in throat size, corresponding to an increase of the P_C. This process resulted in the generation of 970 volumes with the calculated invading fluid distribution, at any given reaction time and throat size, available. The calculation of the volumes required 24h on a desktop PC. In Fig. 5, the calculated invading fluid is displayed in yellow. On the left, the calculated radiographs of the invading fluid for three porosity states during dissolution and three steps of increasing P_C; this provides an example of the difference in the distribution of a non-wetting phase expected at for different alterations of the pore space. On the right, the actual calculated 3D volume rendering of the modeled radiograph in the center is shown, superimposed over the (vertically cut) measured volume of the sample, to provide context.

With this rich dataset spanning both dissolution state and invasion, it is possible to obtain a P_C *surface,* since we can add the extra dimension of reaction time during dissolution. This surface is plotted in Fig. 6, where for each “step” in the P_C surface, a calculated volume of the invading fluid has

been calculated. Three of these volumes are shown, taken from the P_C curve of the volume after 20 hours of reaction, for different throat sizes. From the P_C surface it is possible to appreciate how the entry pressure varies significantly with the extent of the reaction. This is due to a combination of both the increase in porosity in general, but especially to the increase in the largest pore/throat, and more specifically the local thickness values close to the inlet. From the surface plot it is also possible to obtain P_C sections along the reaction extent. If we assume an experimental condition comparable with the experiment and relative drainage model presented in Voltolini et al., 2017, we can follow the evolution of P_C for a throat size value of 105.6 µm (the value found able to simulate the experimental drainage data): in the unreacted sample, the invaded volume would be extremely small, around 1%, while the sample would become more and more prone to be invaded with the evolution of the pore space, ending with an invaded volume (total volume of the sample) by $scCO_2$ of 8.8% i.e. a large fraction of the pore space connected to the inlet. The increase in throat size close to the inlet makes the first step of invasion much easier, and the dissolution along the preferential flowpaths creates large channels where the P_C is low. These pathways provide easy primary access (connectivity) to the other pores with smaller local thickness values, so when the P_C is increased they are progressively invaded.

The channeling effect is also visible from the P_C surface; when looking at the single P_C profiles an evolution of the shape of the single profiles is clear. For the less reacted samples the increase is progressive, with the sudden increase in the invaded volume for small throat size values, meaning that the bulk of the pore space is dominated by small throats, and when the P_C is high enough to overcome the bottlenecks the volume is quickly invaded. The reacted volume exhibits different characteristics; the evolution of channeling systems provides the invading fluid an easy accessible pathway, marked by the growth of a shoulder on the P_C profile. The shoulder appears when the enlarged channels are invaded, early in the process, and subsequently the porosity connected to the main flowpaths by the smaller throats is invaded, generating the increase in invaded volume in the higher P_C part of the curve. These results obtained with the modeling of the drainage process complement the morphologic observations of the tomographic datasets.

3.2. Permeability evolution

Another opportunity provided by the digital rock physics approach is the calculation of the evolution of the single phase permeability of the system during the reaction. Direct permeability measurements on small (mm) samples in complex experimental cells are challenging due to the subtle pressure drop induced by permeable samples and the large effect of tubing runs; in these situations, direct numerical modeling using tomographic data becomes attractive. The method used for this model is based on the direct simulation of Stokes flow, using the model developed by Zuo et al., 2017 (Explained in detail in Appendix A). The goal in this case is to numerically determine the porosity/permeability relationship for this particular dissolution path. In Table 1, both relative and absolute values of permeability and porosity (baseline, the starting unreacted sample = 1) are summarized, with permeability values calculated via the Stokes solver, and porosity values

calculated from the analysis of the tomographic datasets. From these values, we can observe that the value of porosity has close to doubled at the end of the experiment, increasing from 11% to 21%. As is clear from the prior sections however, this change is likely an oversimplification of the system given the heterogeneity of the dissolution process and presence of sub-resolution porosity in the baseline volume.

If we consider the permeability values, we can observe that the permeability at the end of the experiment is 23 times the value of the baseline sample. In Fig. 7 (top) the plots of permeability and porosity are shown. From these curves we can see how the porosity increases significantly in the first stages of the reaction. From the graph, a temporary decrease in the reaction can be seen, visible between t = 16 h and 20 h. The reason for this specific behavior is unclear, and no noticeable issues during the experiment were detected. The permeability values almost constantly increase in the first half of the experiment, followed by a more rapid, exponential growth, at late times as the channeling system further develops. At the bottom of the Fig. 7, three volumes, corresponding to the labels a), b), and c) in the graph above, are shown for different reaction times, with the velocity fields of the fluid displayed in color. At t = 20 h the presence of some channeling features, with faster flow velocities, starts to appear, especially around the inlet zone. At t = 36 h the presence of a channeling system is clear, particularly in the zones closer to the inlet (top). A relevant question is the quantitative relationship between porosity and permeability in this system. Plotting the porosity vs. permeability curve (Fig. 8), we can see a clear pattern. The fit of those values with a power law function is almost perfect.

$$k \propto \phi^{\alpha} \qquad 3)$$

From the equation of the function (3) we can find the exponent α close to 5. This is a value very similar to the one found for a sample with a similar behavior in Menke et al. (2017), and different than the value of 3 used in the Kozeny-Carman relation, as found also in other systems (e.g. Fontainebleau sandstone, in Bourby et al., 1987). This latter example is one of those where the exponent value varies with the porosity, meaning that the fit of the data along the whole porosity interval with a power law function, with a constant α, is not correct. These observations suggest that a sub-scale porosity/permeability relationship might be useful for larger reactive transport models, where the functional form α is dependent on local estimates of Damkhöler and Péclet numbers, thus capturing the non-uniformity of such relationships across different pore-structure evolution paths.

In our sample the value of 5 is constant for all the intervals (no outliers) in the considered porosity interval, as also highlighted by the high quality fit ($R^2 \approx 1$) of the measured data with the plotted function. The values of α for evolving systems have been measured, with a focus on the diagenetic processes (e.g. Bernabé et al., 2003) and it has been found to be rather variable, depending on the sample and processes observed. An experiment involving the dissolution of a compact limestone (McCune et al., 1979) instead found very large values for α (>20). A larger value (α = 13)

was found from a more homogeneously dissolving limestone, measured via dynamic in situ SXR-µCT as presented in Noriel et al. (2005).

4. Conclusions

This work presents observations of pore-structure evolution of a limestone during dissolution induced by a CO_2-rich fluid, followed by a modeling study to quantify likely impacts on hydraulic properties. This topic is of relevance to both GCS and EOR operations, where the variations in the hydraulic properties of the reservoir rock due to geochemical reactions can potentially have a significant impact on flow distribution in the field. We have studied the phenomena at the pore scale using in-situ SXR-µCT, monitoring the evolution of the microstructure of the sample with time, while flowing the reactant, and using the datasets obtained to characterize the kind of pore space evolution, and then model the hydraulic properties of the sample. We have found that the system evolves, developing a channeling dissolution pattern. With time, the dissolution becomes more pronounced along preferential flowpaths. At the beginning of the experiment, the dissolution is more homogeneous and diffuse, when preferential flowpaths are not established and highly reactive material is available. With the increase in extent of the reaction, preferential flowpaths develop and positive feedbacks with dissolution enlarge these features, particularly close to the inlet where the amount of available reactant is higher.

Such an evolution of the morphology of the pore space significant impacts the hydraulic properties of the sample. The modeled P_C curves as a function of reaction extent show a dramatic decrease in entry pressure, coupled with a large increase in invaded volume for a given throat size, as dissolution proceeds. The decrease in entry pressure is explained by the enhanced dissolution close to the inlet; the increase in invaded volume with the reaction at constant throat size (or the equivalent P_C) is easily explained by the development of the large channels along the preferential flowpaths still well connected to the inlet. This channeling effect also has a significant impact on the single-phase permeability of the system. We have calculated the permeability using a Stokes solver and studied its relationship with porosity. While the porosity almost doubles, the increase in permeability of the system at the end of the experiment is 23 times the starting value. A power law fit of the porosity vs. permeability highlights how the increase in permeability is larger than the value predicted by the classic Kozeny-Carman equation, but is consistent with similar experiments in literature (Menke et al., 2017).

We should note that the experiment presented here does not accurately represent the conditions of typical GCS or EOR reservoirs. We focus on the evolution of pore space due to chemical dissolution and its potential impact in different scenarios via a digital rock physics approach. The high flow rates and the high availability of the reactant makes this scenario more similar to a shallow near well bore region, during the injection of CO_2. The large increase in permeability due to this channeling effect could increase injectivity. An important zone to consider would be regions near the well bore which are initially not invaded due to lower permeability; these features could be sensitive to dissolution, particularly if secondary brine transport due to density driven flow were significant. Another relevant

component of the system would be near a seal failure where carbonated brine could be driven by overpressure. In terms of non-wetting fluid mobilization, the generation of channels creates flowpaths where the P_C is significantly decreased, creating preferential pathways where the remobilized non-wetting fluid can move easily.

We have shown the new opportunities opened by coupling in-situ XR-µCT coupled with digital rock physics models. This combination of technologies allows the simulation of difficult or impossible experiments on evolving systems, in this case enabling the quantification of multiphase hydraulic properties during aqueous phase dissolution of a carbonate sample.

Acknowledgements

This work was supported as part of the Center for Nanoscale Control of Geologic CO2 (NCGC), an Energy Frontier Research Center funded by the U.S. Department of Energy, Office of Science, Basic Energy Sciences under Award # DE-AC02-05CH11231. The SXR-µCT experiment was performed with the assistance of Alastair MacDowell and Dula Parkinson at the Advanced Light Source, Beamline 8.3.2, supported by the U.S. DOE Office of Science, Office of Basic Energy Sciences (DE-AC02-05CH11231). Dr. Lin Zuo and Prof. Sally Benson are acknowledged for sharing the Stokes solver code developed at LBNL and Stanford University.

References

Andrä, H., Combaret, N., Dvorkin, J., Glatt, E., Han, J., Kabel, M., Keehm, Y., Krzikalla, F., Lee, M., Madonna, C. and Marsh, M., 2013. Digital rock physics benchmarks—Part II: Computing effective properties. *Computers & Geosciences*, *50*, pp.33-43.

Baritantonaki, A., Bolourinejad, P. and Herber, R., 2017. An experimental study of dolomite dissolution kinetics at conditions relevant to CO2 geological storage. *Petroleum Geoscience*, *23*(3), pp.353-362.

Benson, S., Cook, P., Anderson, J., Bachu, S., Nimir, H.B., Basu, B., Bradshaw, J., Deguchi, G., Gale, J., von Goerne, G. and Heidug, W., 2005. Underground geological storage. *IPCC special report on carbon dioxide capture and storage*, pp.195-276.

Benson, S.M. and Cole, D.R., 2008. CO_2 sequestration in deep sedimentary formations. *Elements*, *4*(5), pp.325-331.

Bernabé, Y., Mok, U. and Evans, B., 2003. Permeability-porosity relationships in rocks subjected to various evolution processes. *Pure and Applied Geophysics*, *160*(5), pp.937-960.

Bourbie, T.O. Coussy, B. Zinszner. 1987. Acoustics of Porous Media. *Gulf Publishing Co, Houston, Texas.*

Carroll, S.A., Iyer, J. and Walsh, S.D., 2017. Influence of Chemical, Mechanical, and Transport Processes on Wellbore Leakage from Geologic CO_2 Storage Reservoirs. *Accounts of Chemical Research*.

Cavanagh, A.J. and Haszeldiner, R.S., 2014. The Sleipner storage site: Capillary flow modeling of a latered CO_2 plume requires fractured shale barriers within the Utsira formation. *International Journal of Greenhouse Gas Control*, *21*, pp. 101-112.

Deng, H., Molins, S., Steefel, C., DePaolo, D., Voltolini, M., Yang, L. and Ajo-Franklin, J., 2016. A 2.5 D reactive transport model for fracture alteration simulation. *Environmental science & technology*, *50*(14), pp.7564-7571.

Deng, H., Voltolini, M., Molins, S., Steefel, C.I., DePaolo, D.J., Ajo-Franklin, J. and Yang, L., 2017. Alteration and erosion of rock matrix bordering a carbonate-rich shale fracture. *Environmental Science & Technology*.

Dierick, M., Masschaele, B. and Van Hoorebeke, L., 2004. Octopus, a fast and user-friendly tomographic reconstruction package developed in LabView®. *Measurement Science and Technology*, *15*(7), p.1366.

Dougherty, R. and Kunzelmann, K.H., 2007. Computing local thickness of 3D structures with ImageJ. *Microscopy and Microanalysis*, *13*(S02), p.1678.

Fredd, C.N. and Fogler, H.S., 1998. Influence of transport and reaction on wormhole formation in porous media. *AIChE journal*, *44*(9), pp.1933-1949.

Gislason, S.R. and Oelkers, E.H., 2014. Carbon storage in basalt. *Science*, *344*(6182), pp.373-374.

Gouze, P. and Luquot, L., 2011. X-ray microtomography characterization of porosity, permeability and reactive surface changes during dissolution. *Journal of contaminant hydrology*, *120*, pp.45-55.

Grgic, D., 2011. Influence of CO2 on the long-term chemomechanical behavior of an oolitic limestone. *Journal of Geophysical Research: Solid Earth*, *116*(B7).

Freire-Gormaly, M., Ellis, J.S., Bazylak, A. and MacLean, H.L., 2015. Comparing thresholding techniques for quantifying the dual porosity of Indiana Limestone and Pink Dolomite. *Microporous and Mesoporous Materials*, *207*, pp.84-89.

Indiana Limestone Handbook; Indiana Limestone Institute of America, 22nd edition, 2007.

Ji, Y., Baud, P., Vajdova, V. and Wong, T.F., 2012. Characterization of pore geometry of Indiana limestone in relation to mechanical compaction. *Oil & Gas Science and Technology–Revue d'IFP Energies nouvelles*, *67*(5), pp.753-775.

Kak, A.C. and Slaney, M., 2001. *Principles of computerized tomographic imaging*. Society for Industrial and Applied Mathematics.

Knackstedt, M.A., Latham, S., Madadi, M., Sheppard, A., Varslot, T. and Arns, C., 2009. Digital rock physics: 3D imaging of core material and correlations to acoustic and flow properties. *The Leading Edge*, *28*(1), pp.28-33.

MacDowell, A.A., Parkinson, D.Y., Haboub, A., Schaible, E., Nasiatka, J.R., Yee, C.A., Jameson, J.R., Ajo-Franklin, J.B., Brodersen, C.R. and McElrone, A.J., 2012, October. X-ray micro-tomography at the Advanced Light Source. In *Proc. SPIE* (Vol. 8506, p. 850618).

McGrail, B.P., Schaef, H.T., Ho, A.M., Chien, Y.J., Dooley, J.J. and Davidson, C.L., 2006. Potential for carbon dioxide sequestration in flood basalts. *Journal of Geophysical Research: Solid Earth*, *111*(B12).

Menke, H.P., Bijeljic, B., Andrew, M.G. and Blunt, M.J., 2015. Dynamic three-dimensional pore-scale imaging of reaction in a carbonate at reservoir conditions. *Environmental science & technology*, *49*(7), pp.4407-4414.

Menke, H.P., Andrew, M.G., Blunt, M.J. and Bijeljic, B., 2016. Reservoir condition imaging of reactive transport in heterogeneous carbonates using fast synchrotron tomography—Effect of initial pore structure and flow conditions. *Chemical Geology*, *428*, pp.15-26.

Mohamed, I.M. and Nasr-El-Din, H.A., 2012, January. Formation damage due to CO2 sequestration in deep saline carbonate aquifers. In *SPE International Symposium and Exhibition on Formation Damage Control*. Society of Petroleum Engineers.

Noiriel, C., Bernard, D., Gouze, P. and Thibault, X., 2005. Hydraulic properties and microgeometry evolution accompanying limestone dissolution by acidic water. *Oil & gas science and technology*, *60*(1), pp.177-192.

Oldenburg, C.M., Stevens, S.H. and Benson, S.M., 2004. Economic feasibility of carbon sequestration with enhanced gas recovery (CSEGR). *Energy*, *29*(9), pp.1413-1422.

Otsu, N., 1979. A threshold selection method from gray-level histograms. *IEEE transactions on systems, man, and cybernetics*, *9*(1), pp.62-66.

Ott, H. and Oedai, S., 2015. Wormhole formation and compact dissolution in single- and two-phase CO2-brine injections. *Geophysical Research Letters*, *42*(7), pp.2270-2276.

Peng, C., Crawshaw, J.P., Maitland, G.C. and Trusler, J.M., 2015. Kinetics of calcite dissolution in CO 2-saturated water at temperatures between (323 and 373) K and pressures up to 13.8 MPa. *Chemical Geology*, *403*, pp.74-85.

Schindelin, J., Arganda-Carreras, I., Frise, E., Kaynig, V., Longair, M., Pietzsch, T., Preibisch, S., Rueden, C., Saalfeld, S., Schmid, B. and Tinevez, J.Y., 2012. Fiji: an open-source platform for biological-image analysis. *Nature methods*, *9*(7), pp.676-682.

Siddiqui, S., Nasr-El-Din, H.A. and Khamees, A.A., 2006. Wormhole initiation and propagation of emulsified acid in carbonate cores using computerized tomography. *Journal of Petroleum Science and Engineering*, *54*(3), pp.93-111.

Silin, D.B. and Patzek, T.W., 2009, January. Predicting relative-permeability curves directly from rock images. In *SPE Annual Technical Conference and Exhibition*. Society of Petroleum Engineers.

Silin, D., Tomutsa, L., Benson, S.M. and Patzek, T.W., 2011. Microtomography and pore-scale modeling of two-phase fluid distribution. *Transport in porous media*, *86*(2), pp.495-515.

Voltolini, M., Kwon, T.H. and Ajo-Franklin, J., 2017. Visualization and prediction of supercritical CO 2 distribution in sandstones during drainage: An in situ synchrotron X-ray micro-computed tomography study. *International Journal of Greenhouse Gas Control*, *66*, pp.230-245.

White, D., 2013. Seismic characterization and time-lapse imaging during seven years of CO_2 flood in the Weyburn field, Saskatchewan, Canada. *International Journal of Greenhouse Gas Control*. *16S*. pp. S78-S94.

Zhang, S., DePaolo, D.J., Voltolini, M. and Kneafsey, T., 2015. CO_2 mineralization in volcanogenic sandstones: geochemical characterization of the Etchegoin formation, San Joaquin Basin. *Greenhouse Gases: Science and Technology*, *5*(5), pp.622-644.

Zuo, L., Ajo-Franklin, J.B., Voltolini, M., Geller, J.T. and Benson, S.M., 2017. Pore-scale multiphase flow modeling and imaging of CO_2 exsolution in Sandstone. *Journal of Petroleum Science and Engineering*, *155*, pp.63-77.

Figure captions

Fig. 1
SEM analysis of the sample. a) Back-scattering electrons imaging of a polished section of the sample. b, c, e) Secondary electrons (SE) imaging of the microstructure of the sample at increasing magnification.

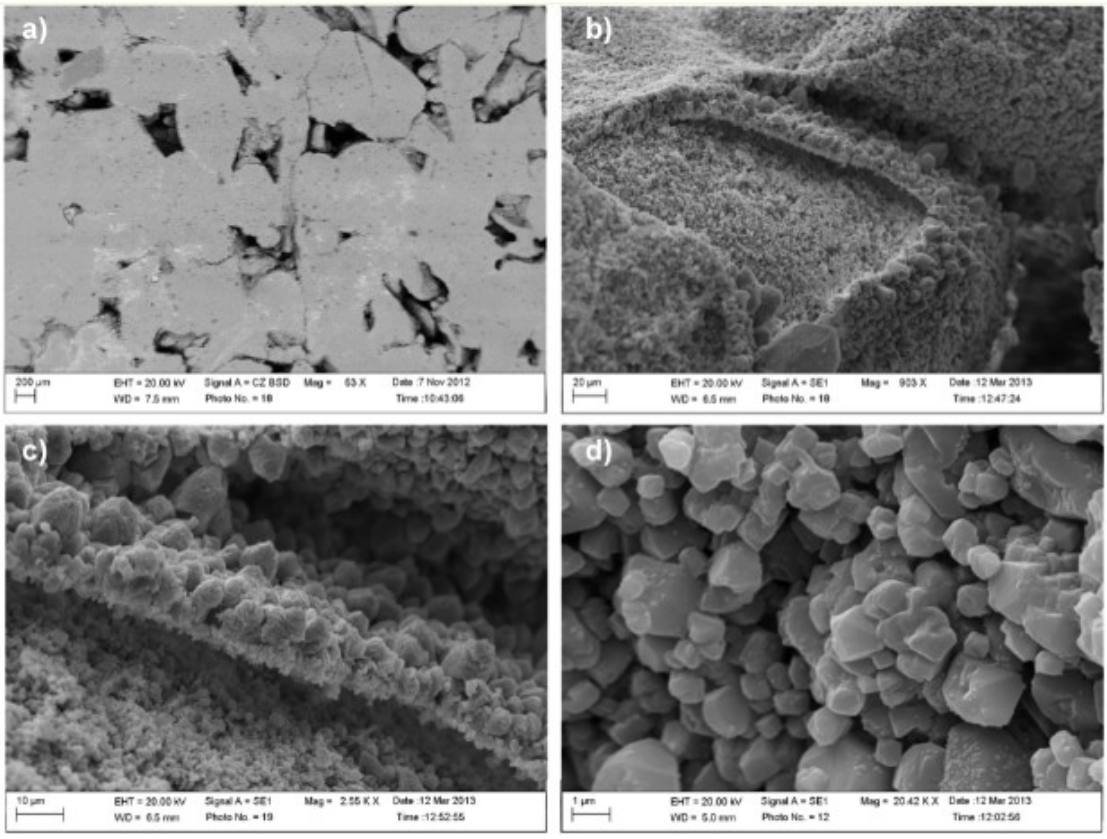

Fig. 2
Volume renderings showing the sequence of the 10 time steps of the experiment, where the sample was measured every 4 hours. The upper half shows a vertical virtual cut (inlet at the top), while the lower half shows a horizontal section about 1 mm under the inlet.

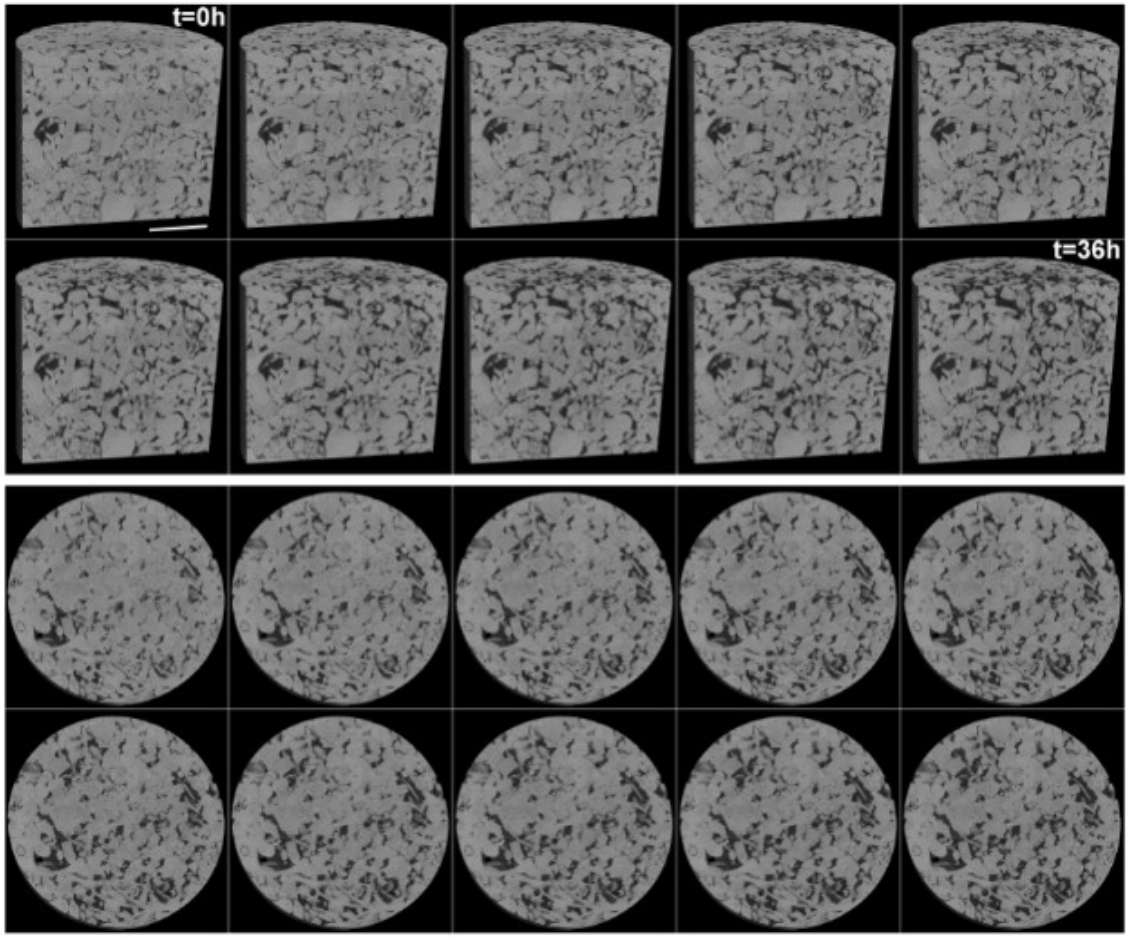

790

Fig. 3
Volume rendering of a vertical thin slab of the sample. The color labeling show the dissolved parts of the sample at the different time steps.

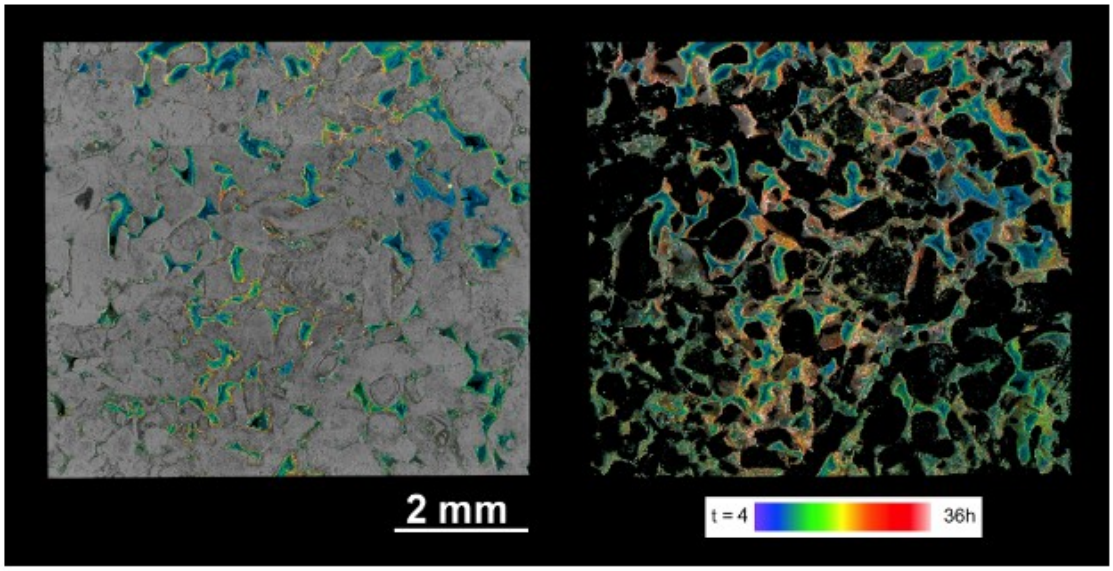

795

Fig. 4
a) Slice-by-slice porosity evolution of the sample. b) Evolution of the local thickness values of the pore space.

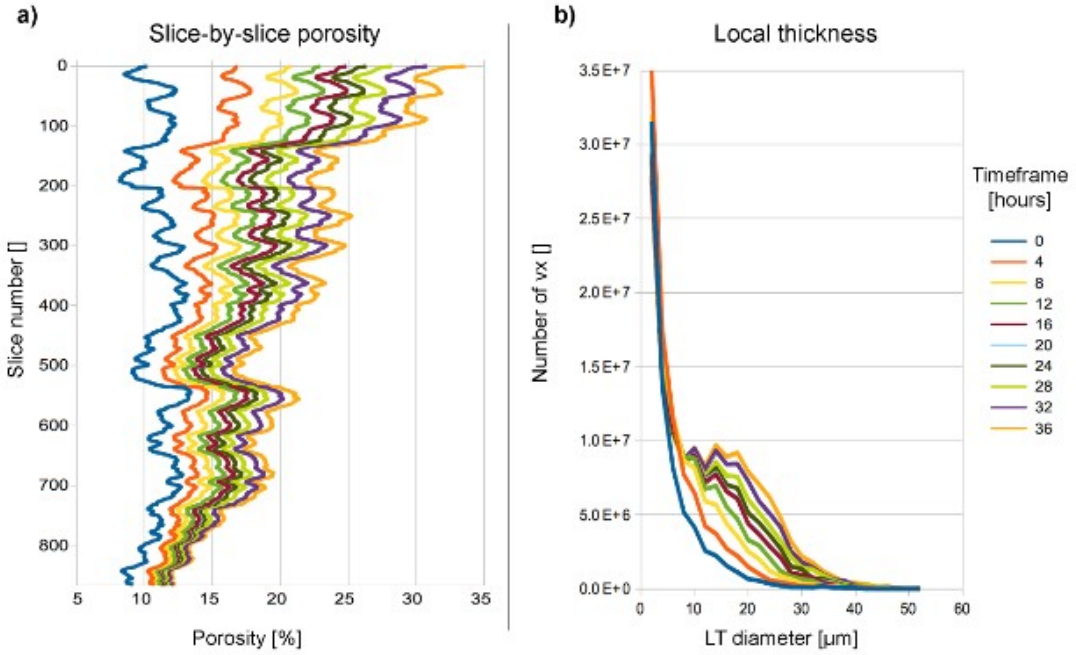

Fig. 5
Calculated radiographs of the invading fluid in the sample for 9 samples at different reaction time and capillary pressure. An example of the 3D calculated volume rendering (in yellow the calculated invading fluid, and in grays the measured and vertically cut volume rendering of the solid phase, are shown) of the sample in its context is shown on the right.

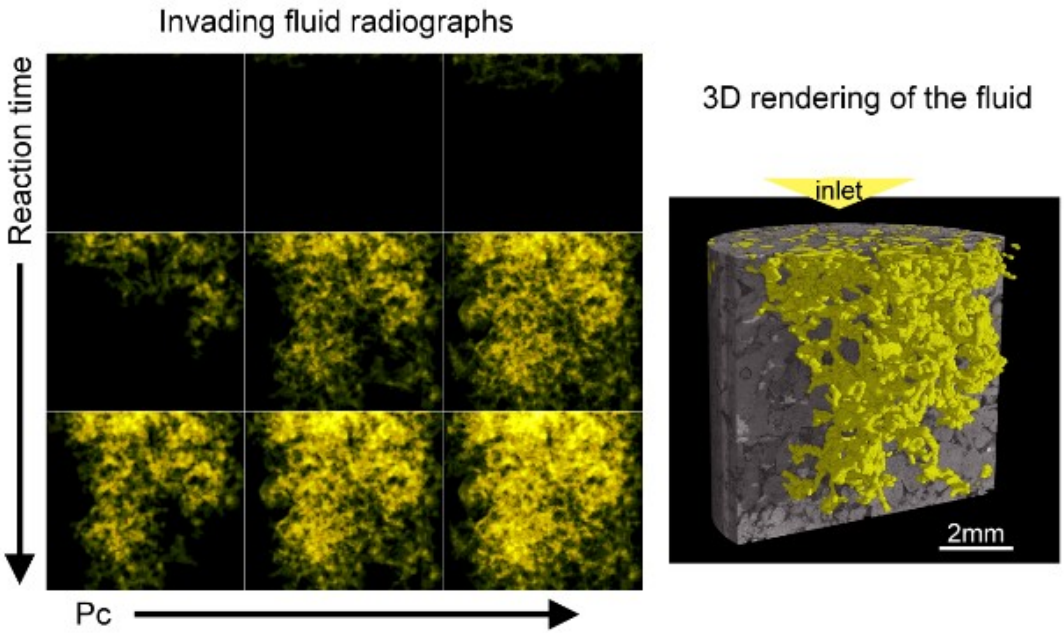

Fig. 6
Drainage curves calculated for the sample at each reaction time. Three volumes, out of the 970 calculated, are shown on the right (the calculated invading fluid in yellow, the measured solids in grays).

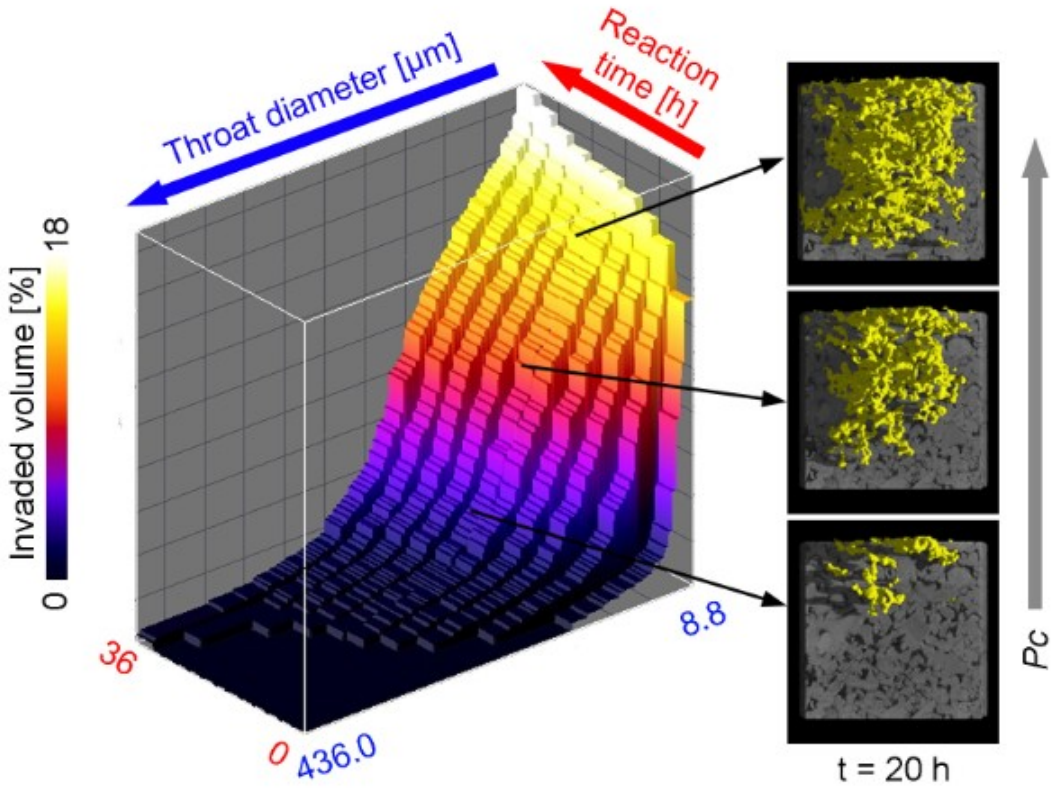

Fig. 7
Top: Evolution plots for the porosity and permeability of the sample during the
820 dissolution. Bottom: three volume renderings of the vertical flow velocity fields for the sample at three different reaction times, as calculated from the Stokes solver, and porosity-corrected to match the experimental setup conditions.

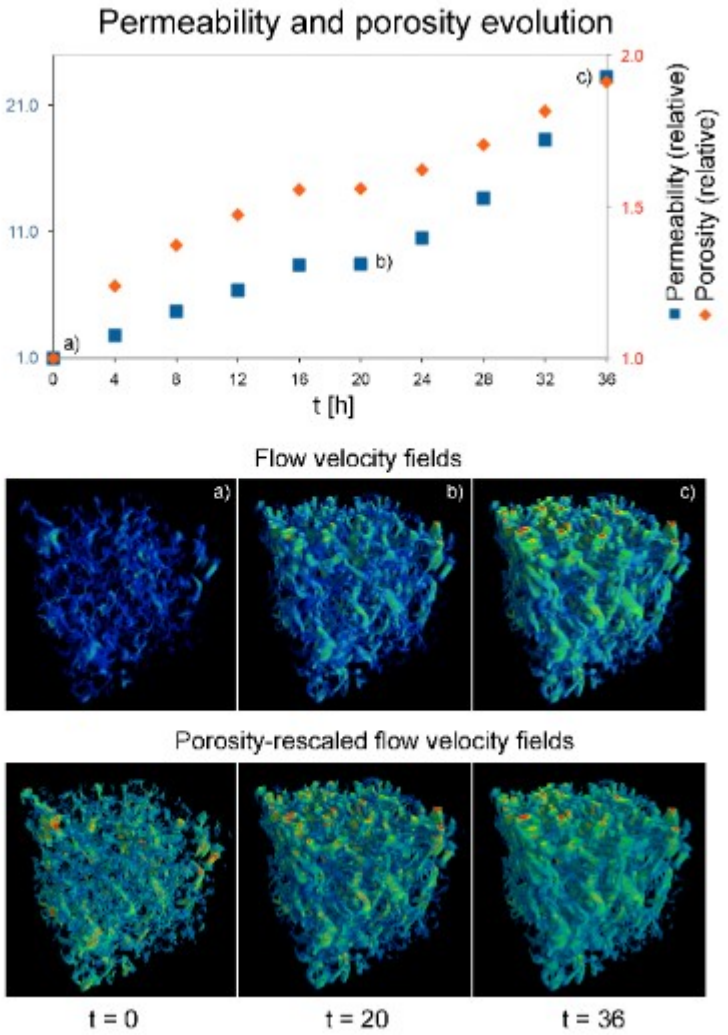

825

Fig. 8
Porosity vs. permeability diagram for the evolving sample, with power law function fit.

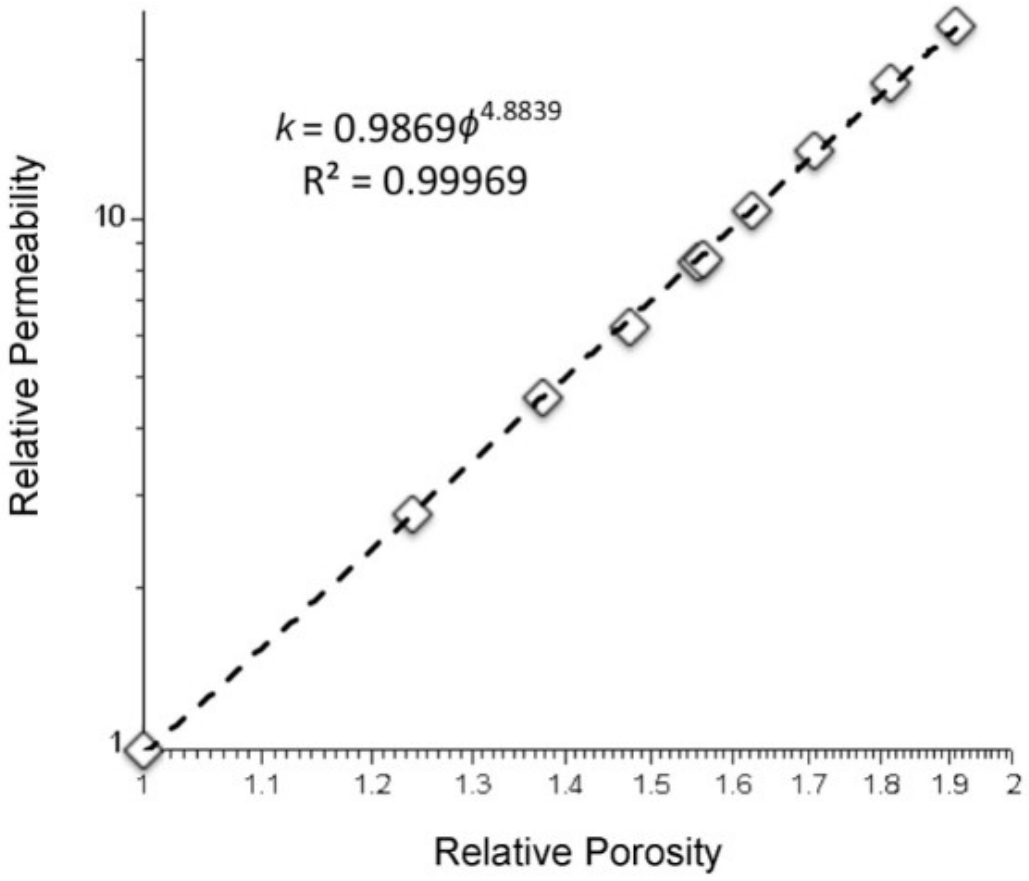
$k = 0.9869\phi^{4.8839}$
$R^2 = 0.99969$
Relative Permeability
10
1
1
1.1
1.2
1.3
1.4
1.5
1.6
1.7
1.8
1.9
2
Relative Porosity

830

Tables

t [h]	Normalized permeability	Normalized porosity	Absolute permeability [Darcy]	Absolute porosity [%]
0	1.00	1.00	1.97	11.0
4	2.79	1.24	5.49	13.6
8	4.67	1.37	9.19	15.1
12	6.35	1.47	12.49	16.2
16	8.37	1.55	16.46	17.1
20	8.45	1.56	16.62	17.2
24	10.50	1.62	20.65	17.8
28	13.66	1.70	26.87	18.8
32	18.31	1.81	36.02	19.9
36	23.30	1.91	45.83	21.0

Table 1.
Summary of the variations of porosity and permeability (as relative values: baseline = 1) and the porosity measured from the tomographic data (% of the total volume) for the sample at different stages of reaction. The permeability has been calculated via Stokes flow solver.